


# Generation of arbitrary cylindrical vector beams using mode-converting metasurfaces

Faris Alsolamy<sup>1,2,\*</sup> and Anthony Grbic<sup>1</sup>

<sup>1</sup>*Department of Electrical Engineering and Computer Science, University of Michigan, Ann Arbor, Michigan 48109-2122, USA*

<sup>2</sup>*King Abdulaziz City for Science and Technology (KACST), Riyadh 12354, Saudi Arabia*

 (Received 21 November 2023; revised 7 May 2024; accepted 24 May 2024; published 1 July 2024)

Cylindrical vector beams (CVBs) are radially polarized or azimuthally polarized beams in the radiative near field. They resist diffraction within the Fresnel zone and exhibit a tighter focusing spot compared to linearly polarized beams. Therefore, CVBs have found several applications, and multiple passive methods have been proposed to generate them. To date, passive antennas have been limited to generating standard CVBs like Gaussian or Bessel beams at microwave frequencies. Therefore, the topic of this paper is twofold. First, a passive method to generate arbitrarily defined CVBs is proposed. Second, the method is applied to realize two experimental CVB antennas. One antenna generates an orthogonal Bessel summation (OBS) beam, while the other generates the well-known radial Gaussian (RG) beam. The OBS beam is a superposition of multiple, weighted Bessel beams. Therefore, it cannot be readily realized using standard CVB antennas. It is unique in that it exhibits zero diffraction loss at a given plane tangential to the aperture, within its Fresnel zone, resulting in maximum coupling between circular apertures within the Fresnel zone. Key to the proposed method of generating CVBs is the spatially dispersive mode-converting metasurface. Unlike conventional metasurfaces, the normal power density does not have to be locally conserved across this metasurface.

DOI: [10.1103/PhysRevApplied.22.014001](https://doi.org/10.1103/PhysRevApplied.22.014001)

## I. INTRODUCTION

An experimental demonstration of what is known today as a cylindrical vector beam (CVB) dates back to 1972 [1,2]. In 1972, Mushiaké *et al.* reported a practical generation of a radially polarized optical beam using a He-Ne gas laser [2]. Subsequently, in 1987, Durnin proposed the nondiffractive properties of the radial Bessel (RB) beam [3]. The RB beam is a classic example of a CVB. It resists diffraction over a finite range within the Fresnel zone of the generating apparatus, known as the nondiffractive range [4–7]. Another classic example of a CVB is the radial Gaussian (RG) beam. The RG beam also incurs minimal diffraction within the Rayleigh length of the beam [8]. In fact, through focusing, the RG beam can attain zero diffraction loss at a particular tangential plane within its Rayleigh length [9].

In 2000, another interesting property of CVBs was reported [10]. It was numerically shown that a tighter focusing spot can be attained with radially polarized beams compared to typical linearly polarized beams. The numerical results in Ref. [10] were experimentally verified in Refs. [11,12].

CVBs can be formally defined as radially or azimuthally polarized beams that solve the exact or the paraxial vector wave equation in free space [13–15]. Due to their diffraction-resisting properties in the radiative near field [8] and the fact that they exhibit a tighter focusing spot compared to similar beams with a homogeneous polarization state [10,11,16], they have found several applications [16]. These applications include imaging and microscopy [17,18], optical trapping [19], laser machining [20], and radiative wireless power transfer [9,21,22].

Following Mushiaké's pioneering work, several passive methods were proposed to generate CVBs. In general, these methods involve the use of polarization conversion devices, where the polarization of more common beams, linearly or circularly polarized beams, is converted to the desired polarization state. A summary of such methods can be found in Ref. [16]. Another method to generate CVBs is to carefully excite the TE<sub>01</sub> mode or TM<sub>01</sub> mode in an optical fiber while suppressing the fundamental HE<sub>11</sub> mode [23–25]. More recent methods to generate CVBs use metasurface technology [7,26–28].

Passive methods of generating CVBs, especially at microwave frequencies, rely on either polarization conversion or single-mode excitation. Both approaches do not provide control over the spatial (equivalently the modal)

\*Corresponding author: [alsolamy@umich.edu](mailto:alsolamy@umich.edu)

distribution of the CVB. As a result, antennas have been solely used to generate CVBs with standard spatial profiles, such as Bessel or Gaussian profiles, since these spatial profiles are natural modes of the employed cavities. This leads to the two following questions:

- (a) Can arbitrarily defined CVBs (CVBs with arbitrary amplitude and phase profiles) be generated using passive devices?
- (b) How can arbitrarily defined CVBs be useful?

Thus, the topic of this paper is twofold. First, a passive method to generate arbitrarily defined, axially symmetric CVBs is proposed. This method relies on mode conversion, rather than polarization conversion as is common in the generation of CVBs. As depicted in Fig. 1, a mode-converting metasurface can be designed to convert the modal distribution of the excitation in a radial cavity to the modal distribution of a desired CVB. The natural modes of radial cavities form a complete orthogonal set. An arbitrarily defined CVB can be expressed as a superposition of these modes. The discussion will be focused more on the practical realization and applications of the proposed method, as its theoretical foundations have been established in Ref. [29]. Second, an antenna is designed to generate a CVB that has been recently shown to be optimal for coupling two circular apertures within the Fresnel zone [9]. The beam is constructed from a superposition of orthogonal Bessel beams with different complex coefficients. The complex coefficients of the orthogonal Bessel beams are optimized to maximize the power transfer between two identical apertures. For convenience, this beam will be referred to as the OBS beam, which stands for “orthogonal Bessel summation.” Additionally, an experimental antenna is realized to generate the well-known RG beam.

Arbitrarily controlling the amplitude and phase distributions of the generated CVB is what differentiates this method from all other methods of generating CVBs. Given this unique property, the proposed method will allow alternative and unexplored CVBs, such as the OBS beam, that can be optimized and tailored to specific applications or functions. Additionally, this method implements a metasurface solution, permitting low-profile devices fabricated using low-cost methods such as PCB processing. Various metasurface devices have been proposed to control both the amplitude and phase of radiated fields. These include modulated metasurface antennas [30,31], omega-bianisotropic metasurfaces [32], paired metasurfaces [33,34], and others [35]. Most of the proposed devices control far-field beams with a spatially homogeneous polarization state (linearly polarized or circularly polarized beams). In contrast, the method proposed here is used to

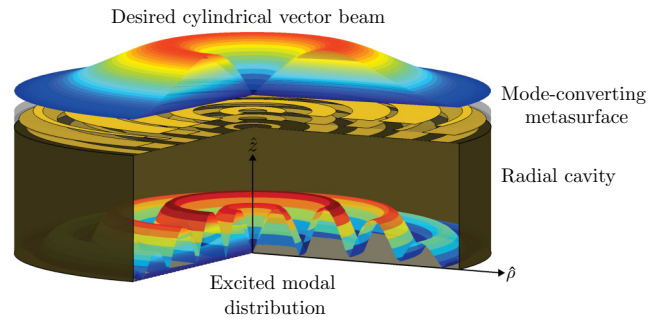


FIG. 1. Generation of arbitrarily defined, axially symmetric cylindrical vector beams by shaping the modal profile inside an excited radial metallic cavity. A cascaded-sheet, mode-converting metasurface is placed atop an excited radial cavity to transform the excited modal distribution to the desired CVB modal profile. The mode-converting metasurface is composed of a stack of spatially varying electric admittance sheets separated by dielectric spacers. The electric admittance sheets are implemented as concentric metallic rings.

control radially polarized beams (spatially nonhomogeneous polarization state) in both far-field and near-field regions

Multilayer mode-converting metasurfaces are central to the antennas proposed in this work that generate CVBs. As explained in Ref. [36,37], they can be designed through optimization, where the impedance profiles of the metasurface layers are optimized to realize a targeted modal transformation. This optimization technique accounts for spatial dispersion due to the finite thickness of the metasurface. Additionally, as discussed in Ref. [38,39], multilayer metasurfaces can be designed to exhibit nonlocal responses, i.e., the normal power density does not have to be locally conserved across the entire metasurface. For these two reasons, the mode-converting metasurface is fundamentally different from other conventional metasurfaces that are designed by defining local boundary conditions, known as, generalized sheet transition conditions (GSTCs) [40,41]. Although, GSTCs have been recently extended to include spatial dispersion [42,43], the optimization technique in Refs. [36,37] appears to be more practical, since the extended GSTCs do not take into account the metasurface thickness.

## II. THE ORTHOGONAL BESSEL SUMMATION (OBS) BEAM FOR MAXIMUM POWER TRANSFER BETWEEN IDENTICAL CIRCULAR APERTURES

This section briefly discusses the OBS beam, since it is an unconventional and recently introduced CVB. As noted, CVBs are known for their diffraction-resisting properties in the radiative near field. For this reason, wireless power transfer using CVBs was the topic of multiple recent papers [9,21,22,44]. In Ref. [22], coupling between

two metasurface-based Bessel beam launchers was considered at microwave frequencies. It was shown that the two launchers can couple through an even or odd free-space mode. In Refs. [9,44], the authors considered coupling between circular apertures supporting several types of CVBs. Notably, it was shown that the OBS beam can transfer power between circular apertures with zero diffraction loss over a range of separation distances [9].

The OBS beam maximizes coupling between two opposing, identical, and radially polarized circular aperture antennas, each backed by a perfect electric conducting (PEC) ground plane, as shown in Fig. 2[9]. According to the surface equivalence principle, each aperture antenna can be represented by an equivalent magnetic current distribution  $\bar{M}$  that radiates radially polarized electric field. The equivalent magnetic current distribution  $\bar{M}$  is evaluated in the absence of the second antenna. As explained in Refs. [45,46] and in Appendix A,  $\bar{M}$  and the fields due to  $\bar{M}$  can be used to find the coupling between the two aperture antennas by performing reaction integrals. A radially polarized OBS beam that maximizes coupling between two circular apertures separated by a distance  $z_s$  can be generated using a circular aperture supporting the following magnetic current distribution  $\bar{M}^{\text{OBS}}$ :

$$\bar{M}^{\text{OBS}} = \sum_{n=1}^N \frac{A_n^{z_s}}{u_n} J_1 \left( \frac{j_n}{R} \rho \right) \hat{\phi}, \quad (1)$$

where,  $j_n$  is the  $n$ th null of the Bessel function of the first kind and order zero,  $R$  is the radius of the physical aperture, and  $u_n = \sqrt{J_1^2(j_n) R^2/2}$ . The complex coefficients  $A_n^{z_s}$  are found through optimization. Although, the optimization procedure was explained in Ref. [9], a summary of

the procedure is provided in Appendix A for the reader's convenience.

It is worth mentioning that the OBS satisfies the condition of maximum coupling between identical circular aperture antennas separated by a distance  $z_s$ , which is given as follows:

$$T(\rho) \bar{H}(\rho, z = z_s) = b T(\rho) \bar{H}^*(\rho, z = 0), \quad (2)$$

where,  $\bar{H}(\rho, z = 0)$  is the tangential propagating magnetic field evaluated at the transmitting aperture. The field  $\bar{H}(\rho, z = z_s)$  is the tangential propagating magnetic field evaluated at the receive aperture ( $z = z_s$ ).  $T(\rho \leq R) = 1$ ,  $T(\rho > R) = 0$  and  $b$  is a complex constant that is related to the coupling coefficient between the two aperture antennas  $\Gamma$  as follows:

$$\Gamma = |b|^2. \quad (3)$$

A proof of the condition given by Eq. (2) and relation (3) is provided in Appendix B. When  $|b| = 1$ , condition (2) guarantees zero diffraction loss and, therefore, maximum power transfer (see Fig. 2). This is in contrast to the conventional Bessel beam, which exhibits minimal, but nonzero, diffraction loss within a specific range known as the nondiffractive range [8,47]. Equation (2) can be translated into an eigenproblem. Using the free-space Green's function, the tangential magnetic fields  $\bar{H}(\rho, z = 0)$ , and  $\bar{H}(\rho, z = z_s)$  in Eq. (2) can be both written in terms of the magnetic current distribution  $\bar{M}^{\text{OBS}}$  in Eq. (1). Therefore, the magnetic current distribution  $\bar{M}^{\text{OBS}}$  of an OBS beam that maximizes the coupling between two apertures separated by a distance  $z_s$  must be the eigenfunction with the maximum eigenvalue of the following integral equation:

$$T(\rho) \int_0^R \bar{M}^{\text{OBS}}(\rho') g_p(\rho'; \rho, z_s) \rho' d\rho' = b T(\rho) \int_0^R (\bar{M}^{\text{OBS}})^*(\rho') g_p(\rho'; \rho, 0) \rho' d\rho', \quad (4)$$

where,  $g_p(\rho'; \rho, z) = \int_0^{2\pi} \sin(k_0 \sqrt{z^2 + \rho^2 + \rho'^2 - 2\rho\rho' \cos(\phi)}) / \sqrt{z^2 + \rho^2 + \rho'^2 - 2\rho\rho' \cos(\phi)} d\phi$  and  $k_0$  is the free-space wave number. Note that the free-space Green's functions have been modified so that only the propagating spectrum is considered when evaluating the fields.

Comparing a Bessel beam to an OBS beam, or even to an RG beam, we notice that the Bessel beam is a natural mode of a uniform radial waveguide. Therefore, it is easy to generate a Bessel beam using a radial cavity. For example, a TM Bessel beam can be generated using a leaky radial cavity covered by a single homogeneous capacitive sheet [7,28], or by using a radial cavity loaded with metallic gratings [48]. On the other hand, generating OBS and RG beams requires the excitation of multiple radial

waveguide modes with appropriate complex amplitudes. Completely controlling the modal distribution in a cavity requires a structure more complicated than a single homogeneous capacitive sheet or metallic gratings. Therefore, OBS and RG beams cannot be generated using standard methods for generating CVBs.

As a final note, the coefficients of the OBS beam can be found by solving the eigenproblem in Eq. (4). However, in this work as explained in Appendix A, the coefficients of

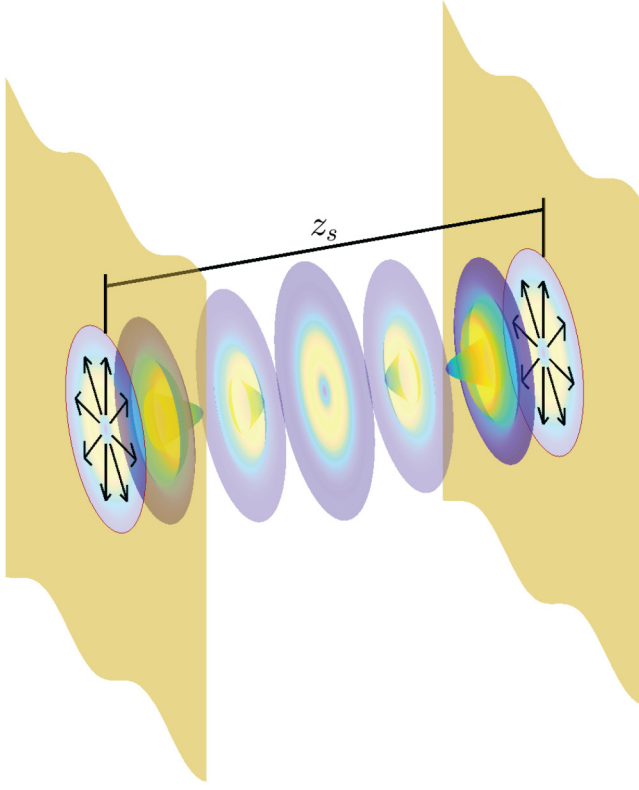


FIG. 2. Two opposing, identical, and radially polarized circular aperture antennas, each backed by a perfect electric conducting (PEC) ground plane. Either aperture antenna is represented by an equivalent magnetic current distribution  $\vec{M}$  that radiates a radially polarized electric field. The slice plots between the apertures represent the tangential component of the propagating magnetic field at different horizontal planes. The color of the slice plots indicates the amplitude of the fields, and the contours of the slice plots indicate the phase of the fields. The propagating magnetic field at the receiving aperture should be the complex conjugate of the magnetic field at the transmitting aperture for maximum coupling between the two apertures.

the OBS beam are found by maximizing the simple form of coupling, Eq. (A19), that is provided in Appendix A.

### III. DESIGN PROCEDURE FOR CVB MODE-CONVERTING METASURFACE ANTENNAS

The proposed CVB mode-converting metasurface antenna consists of three sections: the coaxial feed, the mode-converting metasurface, and the radial cavity (see Fig. 3). This structure is similar to other metasurface antennas that are composed of a metasurface atop a cavity [47,49–51]. The three sections of the antenna can be analyzed and cascaded using modal network theory. In order to demonstrate this, let us recall the modal expansion of radially polarized electric fields in a metallic radial cavity

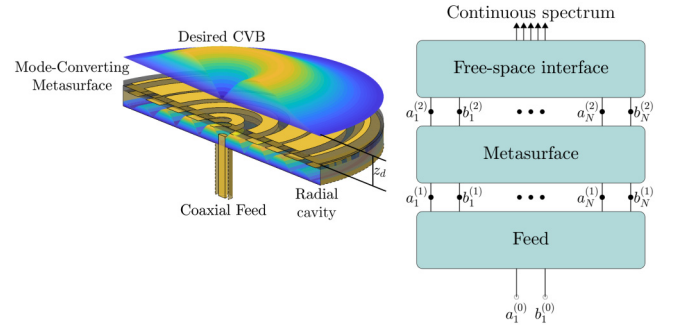


FIG. 3. The proposed CVB mode-converting metasurface antenna. It consists of a mode-converting metasurface backed by a coaxially fed radial metallic cavity. The antenna can be divided into three sections: the metallic cavity, the metasurface, and the feed. Each section can be described using a multiport modal network. The entire antenna can be analyzed and designed by cascading the multiport modal networks of each section. The desired CVB can be formed directly at the cavity’s aperture or at a displaced plane that is  $z_d$  meters away from the aperture.

excited at its center,

$$E_\rho = \sum_{n=1}^N \sqrt{\frac{\eta_n^{\text{TM}}}{u_n^2}} [a_n(z) + b_n(z)] J_1\left(\frac{j_n}{R} \rho\right), \quad (5)$$

where,  $j_n$ , and  $R$  are defined as in Eq. (1),  $u_n$  is defined as in Eq. (1),  $\eta_n^{\text{TM}}$  is the TM wave impedance of the  $n$ th mode. In addition,  $a_n(z)$  and  $b_n(z)$  are the forward and backward modal coefficients, and their  $z$  dependence is given by a propagating and decaying exponential as follows:

$$\begin{aligned} a_n(z) &= a_n e^{-i\left(\sqrt{k_0^2 - \left(\frac{j_n}{R}\right)^2}\right) z}, \\ b_n(z) &= b_n e^{i\left(\sqrt{k_0^2 - \left(\frac{j_n}{R}\right)^2}\right) z}, \end{aligned} \quad (6)$$

where,  $k_0$  is the free-space wave number, and  $a_n$  and  $b_n$  are complex constants. Inside the coaxial feed, only the fundamental TEM mode is assumed.

To proceed, we need to define a set of modes with reference to Fig. 3 as follows. At the input plane of the coaxial feed,  $a_1^{(0)}$ , and  $b_1^{(0)}$  denote the complex coefficients of the incident and reflected coaxial TEM modes, respectively. At the metasurface’s input plane,  $\{a_n^{(1)}\}$ , and  $\{b_n^{(1)}\}$  denote the complex coefficients of the forward and backward  $\text{TM}_{0n}$  cavity modes. Finally, at the metasurface’s output plane (the aperture plane of the antenna),  $\{a_n^{(2)}\}$ , and  $\{b_n^{(2)}\}$  denote the complex coefficients of the forward and backward  $\text{TM}_{0n}$  cavity modes. Now, we can write the

following relations:

$$\begin{bmatrix} b_1^{(0)} \\ [a_1^{(1)}, \dots, a_N^{(1)}]^T \end{bmatrix} = \bar{\bar{S}}_{\text{feed}} \begin{bmatrix} a_1^{(0)} \\ [b_1^{(1)}, \dots, b_N^{(1)}]^T \end{bmatrix} \quad (7)$$

$$\begin{bmatrix} [b_1^{(1)}, \dots, b_N^{(1)}]^T \\ [a_1^{(2)}, \dots, a_N^{(2)}]^T \end{bmatrix} = \bar{\bar{S}}_{\text{MTS}} \begin{bmatrix} [a_1^{(1)}, \dots, a_N^{(1)}]^T \\ [b_1^{(2)}, \dots, b_N^{(2)}]^T \end{bmatrix} \quad (8)$$

$$[b_1^{(2)}, \dots, b_N^{(2)}]^T = \bar{\bar{S}}_{\text{aper}} [a_1^{(2)}, \dots, a_N^{(2)}]^T. \quad (9)$$

In Eq. (7),  $\bar{\bar{S}}_{\text{feed}}$  is the modal scattering matrix of the coaxial-to-cavity junction. It relates the reflected modes on both sides of the junction to the incident modes on both sides of the junction. It can be obtained by applying the mode-matching technique, as in Ref. [22], or it can be calculated using commercial electromagnetic solvers. In Eq. (8),  $\bar{\bar{S}}_{\text{MTS}}$  is the modal scattering matrix of the mode-converting metasurface. Similarly, it relates the reflected modes on both sides of the metasurface to the incident modes on both sides of the metasurface. A detailed discussion on the calculation of  $\bar{\bar{S}}_{\text{MTS}}$  can be found in Ref. [37]. Finally, in Eq. (9),  $\bar{\bar{S}}_{\text{aper}}$  is the modal reflection matrix due to the free-space interface. It can be calculated using the spectral form of the free-space Green's function [29]. From Eqs. (7)–(9), the modal coefficients  $b_1^{(0)}$ ,  $\{a_n^{(2)}\}$ , and  $\{b_n^{(2)}\}$  can be found for a given coaxial excitation  $a_1^{(0)}$ . Recall that,  $\{a_n^{(2)}\}$ , and  $\{b_n^{(2)}\}$  are the modal coefficients evaluated at the output plane of the mode-converting metasurface, which is also the antenna's aperture. So, the electric field at the antenna's aperture ( $0 \leq \rho \leq R$ ) can be written using Eq. (5) as,

$$E_{\text{aper}} = \sum_{n=1}^N \sqrt{\frac{\eta_n^{\text{TM}}}{u_n^2}} [a_n^{(2)} + b_n^{(2)}] J_1 \left( \frac{j_n}{R} \rho \right). \quad (10)$$

To generate a desired CVB, we should first stipulate the electric field over an aperture  $E_{\text{CVB}}$  supporting the desired CVB. Then, we can write  $E_{\text{CVB}}$  in terms of the cavity modes,

$$E_{\text{CVB}} = \sum_{n=1}^N e_n J_1 \left( \frac{j_n}{R} \rho \right). \quad (11)$$

In the optimization, we can define the following objective function:

$$F = |b_1^{(0)}| + \|\bar{\bar{E}}_{\text{CVB}} - \bar{\bar{E}}_{\text{aper}}\|, \quad (12)$$

where,  $\bar{\bar{E}}_{\text{CVB}} = [e_1, \dots, e_N]^T$ , and  $\bar{\bar{E}}_{\text{aper}} = \left[ \sqrt{\eta_1^{\text{TM}}/u_1^2} [a_1^{(1)} + b_1^{(2)}], \dots, \sqrt{\eta_N^{\text{TM}}/u_N^2} [a_N^{(2)} + b_N^{(2)}] \right]^T$  are vectors of

the corresponding coefficients. The admittance profiles of the electric sheets can be optimized to minimize the objective function (12) [29]. Note that, minimizing  $|b_1^{(0)}|$  ensures that the coaxial feed is matched to the cavity.

Forming the desired CVB by directly shaping the cavity's aperture, requires shaping both the propagating and the evanescent spectra. This can be challenging. Alternatively, the desired CVB can be formed at a plane slightly displaced from the aperture, by which the evanescent waves excited by the uppermost sheet of the metasurface become negligible. In this case, the objective function is written in terms of the continuous free-space spectrum of the aperture's electric field and the desired CVB. The continuous free-space spectrum of the aperture's electric field, denoted by  $\tilde{E}_{\text{aper}}$ , can be found by mode matching the discrete cavity modes of the aperture's electric field, given by Eq. (10), with the continuous free-space modes as follows:

$$\tilde{E}_{\text{aper}} = \sum_{n=1}^N \sqrt{\frac{\eta_n^{\text{TM}}}{u_n^2}} [a_n^{(2)} + b_n^{(2)}] L_n(k_\rho), \quad (13)$$

where,  $k_\rho$  is the wave number along the radial direction ( $\hat{\rho}$ ) and  $L_n(k_\rho) = \int_0^R J_1(j_n/R\rho) J_1(k_\rho\rho) \rho d\rho$  which is known in closed form [52]. Similarly, the continuous free space spectrum of the desired CVB, denoted by  $\tilde{E}_{\text{CVB}}$ , can be found by mode matching the discrete cavity modes of the desired CVB, given by Eq. (11), with the continuous free-space modes as follows:

$$\tilde{E}_{\text{CVB}} = \sum_{n=1}^N e_n L_n(k_\rho). \quad (14)$$

As opposed to the discrete cavity modes, which are orthogonal only in the cavity domain ( $0 \leq \rho \leq R$ ), the free-space modes are orthogonal over the entire  $\rho$  space ( $0 \leq \rho \leq \infty$ ).

Let us assume, that we wish the desired CVB to be formed at a displaced plane,  $z_d$  meters away from the aperture, as shown in Fig. 3. Then, we can define the following objective function:

$$F = |b_1^{(0)}| + \int_0^\infty |\tilde{E}_{\text{aper}} - \tilde{E}_{\text{CVB}}| e^{-i(\sqrt{k_0^2 - k_\rho^2})^* z_d} k_\rho dk_\rho, \quad (15)$$

The admittance profiles of the electric sheets can be optimized in order to minimize the objective function in Eq. (15). Minimizing Eq. (15) ensures that the desired CVB will be formed at the specified plane, which is  $z_d$  meters away from the aperture. Again, minimizing  $|b_1^{(0)}|$  ensures that the coaxial feed is matched to the cavity.

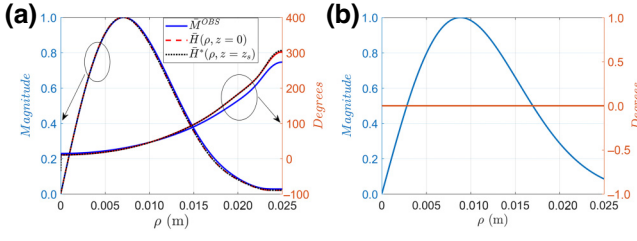


FIG. 4. Normalized amplitude and phase profiles of the magnetic currents supported by the OBS antenna and the RG antenna. (a) An OBS beam that maximizes the coupling between two apertures of radius  $R = 2.5\lambda$  separated by a distance  $z_s = 2.5\lambda$  at 30 GHz.  $\bar{M}^{OBS}$  denotes the profile of the magnetic current,  $\bar{H}(\rho, z = 0)$  denotes the tangential propagating magnetic field at the aperture, and  $\bar{H}(\rho, z = z_s)$  denotes the tangential propagating magnetic field at the plane  $z = z_s$ . We see that  $\bar{H}^*(\rho, z = z_s) = \bar{H}(\rho, z = 0)$ , which is the case of zero diffraction loss and maximum coupling. (b) An RG beam with a uniform phase profile and waist  $w_0 = R/2$ .

#### IV. DESIGN EXAMPLES: OBS BEAM, AND RG BEAM ANTENNAS

In this section, two CVB antennas are realized: one radiates an OBS beam, and the other radiates an RG beam, both operating at 30 GHz. The aperture radius of both antennas is set to  $R = 2.5\lambda$  at the design frequency. The OBS beam radiated by the first antenna maximizes power transfer between two opposing circular apertures placed  $z_s = 2.5\lambda$  away from each other. The beam is constructed from five orthogonal Bessel beams. The aperture of the OBS beam antenna supports a magnetic current  $\bar{M}^{OBS}$  of the following form:

$$\bar{M}^{OBS} = \sum_{n=1}^5 \frac{A_n^{z_s}}{u_n} J_1 \left( \frac{j_n \rho}{R} \right) \hat{\phi}, \quad (16)$$

where,  $j_n$  is the  $n$ th null of the Bessel function of the first kind and order zero,  $R$  is the radius of the physical aperture,  $u_n$  is defined as in Eq. (1), and  $z_s$  denotes the separation distance between the apertures. The complex coefficients  $A_n^{z_s}$  are found using the optimization procedure summarized in Appendix A [9]. The coefficients are optimized to maximize coupling at a separation distance  $z_s = 2.5\lambda$ . The complex coefficients of the considered OBS beam, shown in Fig. 4(a), are given in Table I. For maximum coupling, the OBS beam satisfies the condition given by Eq. (2), where  $b = 0.9983 \angle -35^\circ$ .

The second antenna design generates an RG beam with a uniform phase distribution. The aperture of the RG beam antenna supports a magnetic current  $\bar{M}^{RG}$  of the following form:

$$\bar{M}^{RG} = \sqrt{2} \frac{\rho^2}{w_0^2} e^{-\frac{\rho^2}{w_0^2}} \hat{\phi}, \quad (17)$$

TABLE I. Complex coefficients of  $\bar{M}^{OBS}$ , where  $z_s = 2.5\lambda$  at 30 GHz [53].

$A_1^{z_s}$	$0.4411 \angle 67.8474^\circ$
$A_2^{z_s}$	$0.7867 \angle 44.3187^\circ$
$A_3^{z_s}$	$0.4222 \angle -1.5983^\circ$
$A_4^{z_s}$	$0.0911 \angle -78.7668^\circ$
$A_5^{z_s}$	$0.0059 \angle 136.1688^\circ$

where,  $w_0 = R/2 = 1.25\lambda$  at 30 GHz. The amplitude and the phase distributions of the RG beam are shown in Fig. 4(b). Similar to the magnetic current  $\bar{M}^{OBS}$ , the magnetic current  $\bar{M}^{RG}$  can be expanded in terms of the cavity modes as follows:

$$\bar{M}^{RG} = \sum_{n=1}^5 \frac{A_n^{RG}}{u_n} J_1 \left( \frac{j_n \rho}{R} \right) \hat{\phi}. \quad (18)$$

For the sake of comparison with the OBS beam, the first five complex coefficients of  $\bar{M}^{RG}$  are shown in Table II.

Both antennas comprise a cascaded-sheet mode-converting metasurface that is backed by a coaxially fed metallic radial cavity, as shown in Fig. 5(a). The cavity, the coaxial connector, and the metasurface's dielectric spacers are all the same for both antennas. Antenna dimensions are provided in Fig. 5. It should be noted that, the total thickness of the mode-converting metasurface is  $4.54$  mm, which is  $0.46\lambda$  at 30 GHz. An additional step discontinuity was introduced in the radial cavity to physically support the mode-converting metasurface, as shown in Fig. 5(a). As shown in Fig. 5(b), the mode-converting metasurface consists of four electric admittance sheets separated by dielectric spacers. In the presented examples, Astra MT77 of thickness  $0.03''$  ( $\epsilon_r = 3, \tan \delta = 0.0017$ ) was assumed for the dielectric spacers. The admittance profile of the  $m$ th sheet is denoted by  $Y_m(\rho)$ , where  $Y_1(\rho)$  indicates the sheet that is closest to the coaxial feed. The metallic pattern of the  $m$ th sheet can be found from its admittance profile  $Y_m(\rho)$  through scattering measurements [55,56].

The design process for both antennas can be split into two consecutive steps. In the first step, the sheets' admittance profiles needed for a specific CVB are found through optimization, as discussed in Sec. III. The second step involves the realization of the optimal admittance profiles

TABLE II. Complex coefficients of  $\bar{M}^{RG}$ ; the first five coefficients are shown [54].

$A_1^{RG}$	$0.7739 \angle 0^\circ$
$A_2^{RG}$	$0.6305 \angle 0^\circ$
$A_3^{RG}$	$0.0571 \angle 0^\circ$
$A_4^{RG}$	$0.0131 \angle 0^\circ$
$A_5^{RG}$	$0.0073 \angle 180^\circ$

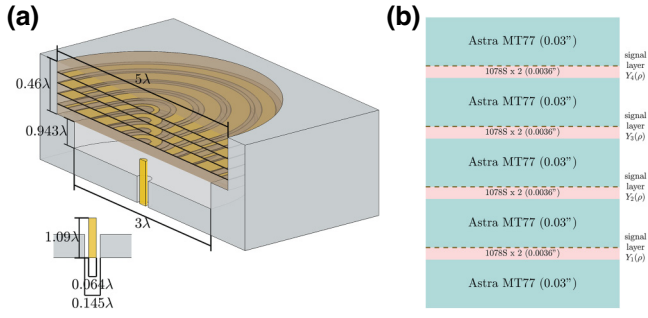


FIG. 5. Dimension of the metasurface antenna used to generate the design examples. (a) Cavity and feed dimensions, (b) mode-converting metasurface cross section.

with patterned metallic rings. First, the electric admittance sheets of the metasurfaces are discretized uniformly into 15 annuli, as shown in Fig. 6(a). Each annulus (cell) has a width equal to  $L = 2.5\lambda/15$ . Therefore, the admittance profile of the  $m$ th sheet  $Y_m(\rho)$ , can be written as a piecewise function,

$$Y_m(\rho) = \begin{cases} iy_1^m & 0 < \rho < \frac{R}{15} \\ iy_2^m & \frac{R}{15} < \rho < \frac{2R}{15} \\ \vdots & \\ iy_{15}^m & \frac{14R}{15} < \rho < R, \end{cases} \quad (19)$$

where,  $R = 2.5\lambda$ , and  $y_{\{1,2,\dots,15\}}^m$  are all real positive numbers. As a result,  $Y_m(\rho)$  are capacitive lossless sheets. Next, the *interior-point* algorithm within the built-in MATLAB function *fmincon* is used to optimize the admittance profiles of the electric sheets. In the OBS example, the beam was formed directly over the aperture. Therefore, the objective function defined by Eq. (12) was minimized to design the OBS beam antenna. In the RG example, the beam was formed at a slightly displaced plane from the aperture ( $z_d = \lambda$ ). So, the objective function defined by Eq. (15) was minimized to design the RG beam antenna. The optimal admittance profiles for both antennas are shown in Figs. 6(b) and 6(c). These optimal admittance profiles can be realized as concentric metallic rings, as shown in Fig. 7(a). In the presented examples, the number of metallic rings per sheet is 15. So, each admittance annulus of each electric sheet is realized with a single metallic ring. A design curve that maps the filling factor of a metallic ring to its admittance can be extracted through simulated scattering measurements, as explained in Refs. [37,55]. See Fig. 7(a) for the definition of the filling factor. The design curve for a metallic ring is shown in Fig. 7(b).

The full-wave solver ANSYS-HFSS was used to verify the performance of the designed OBS and RG beams antennas. The optimal admittance sheets and their metallic ring implementations have been simulated for each antenna. Figure 8 shows the results of the simulation,

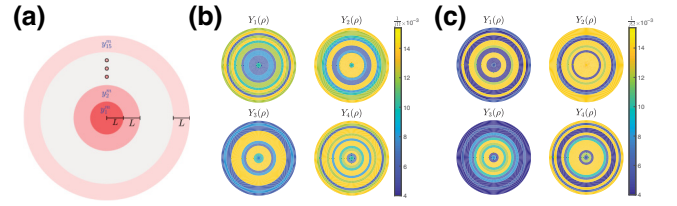


FIG. 6. Discretized admittance profiles of the electric sheets comprising the mode-converting metasurface. (a) The  $m$ th electric admittance sheet  $Y_m(\rho)$  discretized into 15 concentric annuli, where  $y_n^m$  is the admittance of the  $n$ th annulus. (b) The optimal admittance profile needed to generate the OBS beam shown in Fig. 4(a). (c) The optimal admittance profile needed to generate the RG beam shown in Fig. 4(b).

where Desired denotes the desired CVB, Sheets denotes ANSYS-HFSS results for the optimal idealized sheet case, and Patterned denotes ANSYS-HFSS results for the patterned design of metallic rings. For the OBS beam antenna,  $\vec{H}(\rho, z = 0)$  denotes the tangential propagating magnetic field at the aperture, and  $\vec{H}(\rho, z = z_s)$  denotes the tangential propagating magnetic field at the plane  $z = z_s$ , where  $z_s = 2.5\lambda$ . Figures 8(a) and 8(b) show the OBS antenna results. We can see from both figures that the electric field radiated by the Sheet and the Patterned designs agree with the desired fields. Furthermore, we see that  $\vec{H}(\rho, z = 0) = \vec{H}^*(\rho, z = z_s)$  satisfying the condition for maximum coupling. Figures 8(c) and 8(d) show the RG antenna results at a displaced plane ( $z_d = \lambda$ ). Again, we see from both figures that the electric field radiated by the Sheet and the Patterned designs agree with the desired fields. Also, the reflection coefficients calculated using ANSYS-HFSS for both antennas are below  $-20$  dB for the Sheet design. For the Patterned design, the reflection coefficients calculated using ANSYS-HFSS for both antennas are below  $-17$  dB. The results reported in Fig. 8 show that the proposed mode-converting metasurface can be used to design low-profile antennas that generate axially symmetric CVBs.

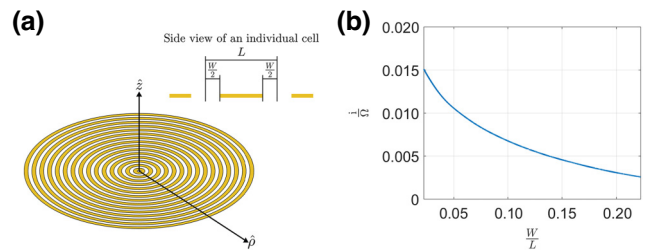


FIG. 7. Realization of the optimal capacitive admittance sheets as concentric metallic rings. (a) Perspective and side views of the concentric metallic rings. The side view shows a single ring that has a filling factor that is equal  $Ff = W/L$ . (b) The design curve for the metallic rings. The curve maps the admittance of the rings to their filling factor.

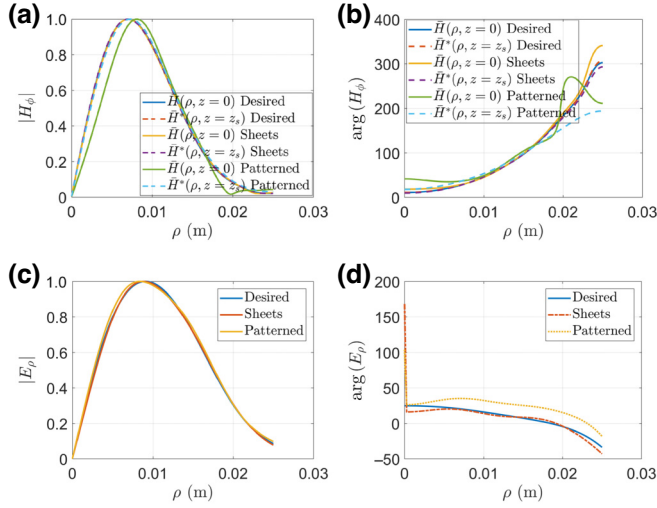


FIG. 8. Simulated fields of the OBS and RG antennas using the full-wave solver ANSYS-HFSS. Desired denotes the fields of the desired CVB, Sheets denote ANSYS-HFSS simulated fields for the optimal idealized sheet design, and Patterned denotes ANSYS-HFSS simulated fields for the patterned metallic rings. (a) The normalized amplitude of the tangential propagating magnetic fields radiated by the OBS antenna. (b) The phase distributions of the tangential propagating magnetic fields radiated by the OBS antenna. (c) The normalized amplitude of the electric fields radiated by the RG antenna. (d) The phase distributions of the electric fields radiated by the RG antenna. In (a),(b)  $\vec{H}(\rho, z = 0)$  denotes the tangential propagating magnetic field at the aperture, and  $\vec{H}(\rho, z = z_s)$  denotes the tangential propagating magnetic field at the plane  $z = z_s$ , where  $z_s = 2.5\lambda$ . In (c),(d) the electric fields are evaluated at a displaced plane  $z = z_d$ , where  $z_d = \lambda$ .

Lastly, the coupling between two opposing and perfectly aligned OBS antennas was calculated using ANSYS-HFSS for the Sheets design and the Patterned design for a separation distance  $z_s = 2.5\lambda$  at 30 GHz. Each OBS antenna was excited and terminated using a matched wave port. The transmission coefficient between the two antennas' ports  $S_{12}$  or equivalently  $S_{21}$  can be used to write the coupling coefficient  $\Gamma$  between the two antennas as follows:

$$\Gamma = |S_{12}|^2. \quad (20)$$

Furthermore, since the simulation assumes no copper or material losses, the normalized diffraction losses coefficient  $Ld$  (which is the ratio between the diffracted power and the total input power) can be calculated as follows:

$$Ld = 1 - |S_{12}|^2 - |S_{11}|^2, \quad (21)$$

where,  $S_{11}$  is the reflection coefficient at any of the two antennas' ports. The simulated coupling coefficient between the two antennas are given in Table III, along with the diffraction losses for the Sheets design and the Patterned design. The results in Table III show that the

TABLE III. The coupling coefficient and the normalized diffraction losses coefficient  $Ld$   $\Gamma$  between two OBS antennas separated  $z_s = 2.5\lambda$  at 30 GHz [57].

	$\Gamma$	$Ld$
Sheets design	0.961	0.039
Patterned design	0.928	0.071

OBS antenna can transmit power efficiently with minimum diffraction losses within the radiative near-field zone.

## V. MEASUREMENTS

In the previous section, RG beam and OBS beam antennas were designed using the method proposed in this paper. The RG antenna was fabricated and the measurement results of the fabricated prototype are discussed in this section. The fabrication process and the measurement setup are presented in Appendix C. Figure 9 shows the reflection coefficient as a function of frequency. We see that the resonance frequency shifted from 30 GHz to approximately 29.5 and 30.4 GHz, which corresponds to 1.6% and 1.2% shift in the frequency. At the design frequency, the reflection coefficient is slightly less than  $-5$  dB. The mode-converting metasurface is designed to perform two functions at the operating frequency: establish the desired CVB and impedance match the feed to the cavity. However, fabrication inaccuracies shifted the desired CVB to one frequency and the impedance matching to different frequencies. Based on the near-field and far-field measurements, we observe that the desired CVB was established at 30.155 GHz, although the antenna is matched at two different frequencies (29.5 and 30.4 GHz).

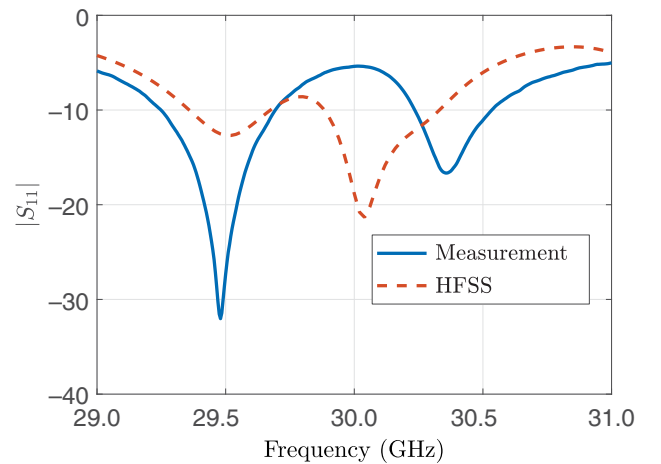


FIG. 9. The measured and simulated (using the commercial full-wave solver ANSYS-HFSS) reflection coefficient ( $|S_{11}|$ ) as a function of frequency.



Figure 10 shows the measured near and far fields at the shifted frequency 30.155 GHz vs the theoretically predicted (Desired) and simulated (ANSYS-HFSS) near and far fields at the design frequency 30 GHz. In Fig. 10(a), the normalized amplitude of the normal component of the electric field  $|E_z|$  has been measured using a coaxial probe at a plane that is  $\lambda$  away from the aperture. The component  $|E_z|$  has been measured along two orthogonal axes ( $y = 0$ ) and ( $x = 0$ ). Along both axes we observe a symmetrical beam, which is expected due to the symmetry of the structure. Additionally, we see that the measured beam for both axes agree with the profile of the desired and simulated RG beam. Figures 10(b) and 10(c) show the normalized amplitudes of the tangential component of the electric field  $E_\rho$  measured at multiple planes tangential to the antenna aperture. In Fig. 10(b), the electric field is measured at 30.155 GHz along the horizontal axis (denoted  $y = 0$ ). The beam expands (diverges with distance) as a Gaussian beam. In Fig. 10(c), the electric field is measured at 30.155 GHz along the vertical axis (denoted  $x = 0$ ). Again, the beam expands (diverges with distance) as a Gaussian beam. Along both axes, we observe a nearly perfect symmetrical beam, which is expected due to the azimuthal symmetry. Figures 10(d) and 10(e) show the phase of the tangential component of the electric field  $E_\rho$  measured along the horizontal and vertical axes, respectively. Again, the phase profiles are symmetric, as expected. Moreover, the phase profiles expand spherically. The antenna far field can be measured using the measured tangential component of the electric field in the near field.

Figure 10(f) shows the measured far field of the antenna at the frequency 30.155 GHz along the horizontal ( $\phi = 0$ ) and vertical ( $\phi = \pi/2$ ) planes. We see good agreements between the measured far field and the simulated (ANSYS-HFSS) far field. Some asymmetries can be observed in the measured far field as shown in the enlarged inset in Fig. 10(f). This is attributed to slight misalignment between the metasurface layers. The measured directivity of the antenna at 30.155 GHz is  $D = 16.5$  dB. The antenna's realized gain is  $G_r = 13.34$  dB, and the antenna's gain is  $G = 14.42$  dB. The efficiency of the antenna, defined as the ratio between the gain and the directivity, is 62%.

## VI. CONCLUSION

The contribution of this work is twofold. First, a passive method to generate cylindrical vector beams (CVBs) with arbitrarily defined amplitude and phase profiles is proposed and experimentally demonstrated. This method relies on mode conversion rather than polarization conversion, as is common in the generation of CVBs. Second, this method is applied to design two CVB antennas. One antenna generates an orthogonal Bessel summation

(OBS) aperture, the optimal aperture illumination for circular apertures. This beam is a superposition of multiple weighted Bessel beams. Therefore, it cannot be readily realized using standard CVB antennas. The other antenna generates the well-known radial Gaussian (RG) beam.

Two design examples are presented. The first design radiates a radial Gaussian (RG) beam, while the second example radiates an orthogonal Bessel summation (OBS) beam. Both antennas were designed at 30 GHz. The performance of both antennas was verified using the commercial full-wave solver ANSYS-HFSS. Furthermore, the RG antenna was prototyped. The fabrication process and the measured performance of the prototype were reported and discussed.

Future work includes the fabrication of the proposed OBS antenna. This antenna can be used to design wireless power-transfer systems that operate in the Fresnel zone, introducing another generation of wireless power-transfer systems.

## ACKNOWLEDGMENT

Dr. Alsolamy acknowledges the support of the KAUST Ibn Rushd Postdoctoral Fellowship. He is grateful for the financial assistance provided, which enabled the completion of this research.

## APPENDIX A: OPTIMIZATION PROCEDURE FOR THE OBS BEAM COEFFICIENTS

As discussed in Sec. II, the OBS beam maximizes power transfer between two identical circular aperture antennas for a given separation distance  $z_s$ . It is constructed as a superposition of orthogonal Bessel beams, each of which is a natural mode of a cylindrical waveguide. The complex coefficients of the constitutive Bessel beams are found through optimization. The optimization procedure is presented here.

To start, let us recall the closed-form expression for the coupling between two identical circular aperture antennas, where one is transmitting and the other is receiving, as shown in Fig. 2,

$$\Gamma = \frac{|\langle R \rangle|^2}{16P^2}, \quad (\text{A1})$$

where,  $\langle R \rangle$  is the electromagnetic reaction between the two aperture antennas and  $P$  is the total power radiated by the transmitting antenna [46,58]. Electromagnetic reaction is a measure of coupling between two electromagnetic emitters [59] and can be written as,

$$\langle R \rangle = \iint_S (\vec{M} \cdot \vec{H}(\rho, z = z_s)) dS, \quad (\text{A2})$$

where,  $\vec{M}$  is the equivalent magnetic current distribution to the receive antennas. As defined in Eq. (2), the

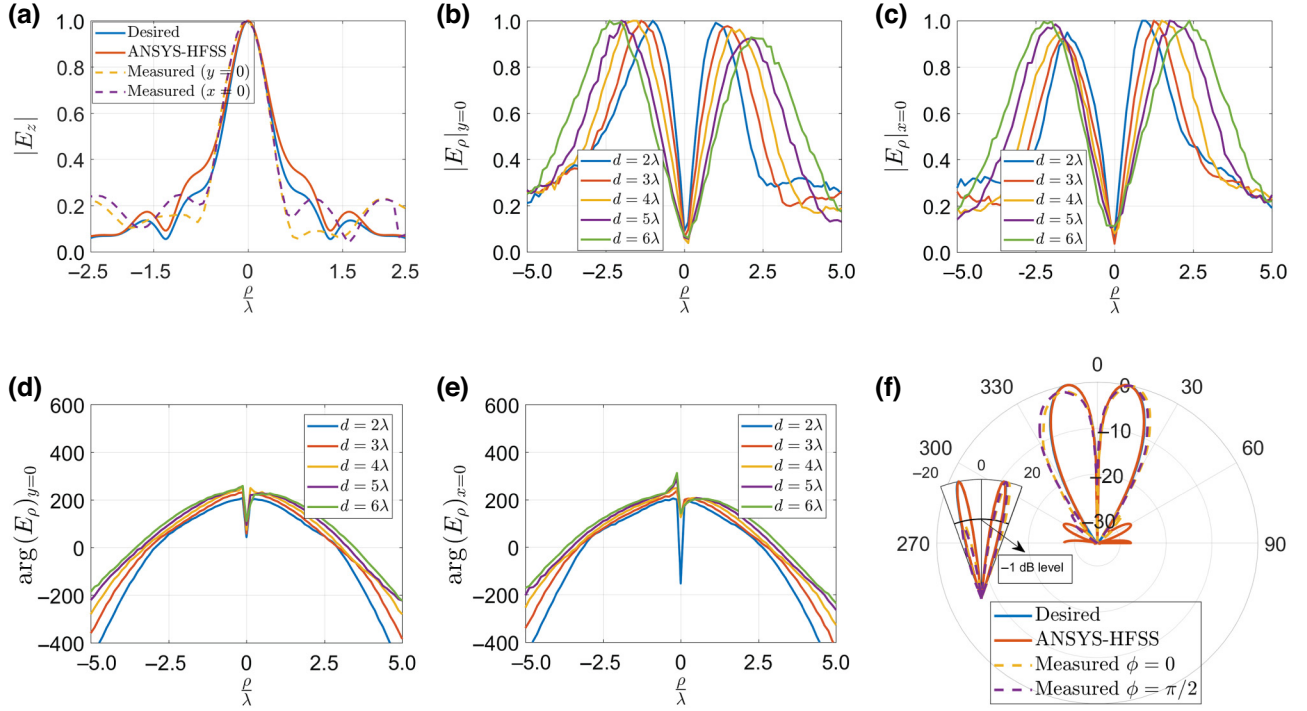


FIG. 10. Measurements of the RG antenna prototype. The fields are measured at the shifted frequency 30.155 GHz and at multiple planes tangential to the antenna aperture. The normal component of the electric field  $E_z$  is measured at a plane that is  $\lambda$  away from the aperture. The measurement planes for the tangential component of the electric field  $E_\rho$  are  $d = 2\lambda$ ,  $d = 3\lambda$ ,  $d = 4\lambda$ ,  $d = 5\lambda$ , and  $d = 6\lambda$  away from the aperture. (a) The theoretically predicted (desired), simulated (ANSYS-HFSS), and measured normalized amplitudes of the normal component of the electric field  $E_z$  at a plane that is  $\lambda$  away from the aperture. The fields are measured along two orthogonal axes: the horizontal axis ( $y = 0$ ) and the vertical axis ( $x = 0$ ). (b) The normalized amplitude of the tangential component of the electric field  $E_\rho$  along the horizontal axis ( $y = 0$ ). (c) The normalized amplitude of the tangential component of the electric field  $E_\rho$  along the vertical axis ( $x = 0$ ). (d) The phase distributions of the tangential component of the electric field  $E_\rho$  along the horizontal axis ( $y = 0$ ). (e) The phase distributions of the tangential component of the electric field  $E_\rho$  along the vertical axis ( $x = 0$ ). (f) The theoretically predicted (desired), simulated (ANSYS-HFSS) and measured far-field radiation patterns along the horizontal ( $\phi = 0$ ) and vertical ( $\phi = \pi/2$ ) planes. Note that the desired pattern is the same along both planes because of the azimuthal symmetry. For clarity, the inset shows the pattern from  $-20^\circ$  to  $20^\circ$ . Some asymmetries in the beam can be observed in the inset. The measurement probe in (b),(d) is  $\hat{x}$  polarized. The measurement port in (c),(e) is  $\hat{y}$  polarized. The far-field pattern in (f) is computed using measured  $\hat{x}$ -polarized and  $\hat{y}$ -polarized near fields. In (a),(f) the theoretically predicted and simulated results are at the design frequency 30 GHz.

field  $\vec{H}(\rho, z = z_s)$  is the tangential propagating magnetic evaluated at the receive aperture ( $z = z_s$ ). The equivalent magnetic current distribution  $\vec{M}$  and the magnetic field  $\vec{H}(\rho, z = z_s)$  are found in the absence of the other antenna [45,46]. The integral is over the area of the receive aperture ( $S$ ). The radiated power  $P$  can be written as,

$$P = \frac{1}{4} \iint_S \vec{M} \cdot \vec{H}^*(\rho, z = 0) dS, \quad (\text{A3})$$

where, the field  $\vec{H}(\rho, z = 0)$  is the tangential propagating magnetic field evaluated at the transmitting aperture ( $z = 0$ ), as defined in Eq. (2).

To proceed, we expand the magnetic current distribution  $\vec{M}$  as in Eq. (1),

$$\vec{M} = \sum_{n=1}^N \frac{A_n}{u_n} J_1 \left( \frac{j_n}{R} \rho \right) \hat{\phi}, \quad (\text{A4})$$

where,  $j_n$  is the  $n$ th null of the Bessel function of first kind and order zero,  $R$  is the radius of the physical aperture, and  $u_n = \sqrt{J_1^2(j_n) R^2 / 2}$ . Also, the magnetic field  $\vec{H}(\rho, z = z_s)$  in Eq. (A2), can be expanded similarly,

$$\vec{H}(\rho, z = z_s) = \sum_{n=1}^N \frac{B_n}{u_n} J_1 \left( \frac{j_n}{R} \rho \right) \hat{\phi}. \quad (\text{A5})$$

Substituting Eq. (A4), and Eq. (A5) into Eq. (A2), we have,

$$\langle R \rangle = 2\pi \sum_{n=1}^N A_n B_n. \quad (\text{A6})$$

Recall that the magnetic field  $\bar{H}(\rho, z = z_s)$  can be related to the magnetic current distribution  $\bar{M}$  through the spectral form of the free-space Green's function as follows:

$$\bar{H}(\rho, z = z_s) = \frac{k_0}{\eta_0} \int_0^{k_0} \frac{e^{-ik_z z_s}}{k_z} \tilde{M}(k_\rho) J_1(k_\rho \rho) k_\rho dk_\rho, \quad (\text{A7})$$

where,  $k_0$  is the free-space wave number,  $\eta_0$  is the characteristic impedance of free space,  $k_z = \left(\sqrt{k_0^2 - k_\rho^2}\right)^*$ ,  $z_s$  is the separation distance between the apertures and

$$\tilde{M}(k_\rho) = \int_0^R \bar{M} J_1(k_\rho \rho) \rho d\rho.$$

Substituting Eqs. (A4), (A5) into Eq. (A7) and exploiting the Bessel functions orthogonality, we have

$$B_n = \frac{k_0}{\eta_0 u_n} \int_0^{k_0} \frac{e^{-ik_z z_s}}{k_z} \sum_{m=1}^N \frac{A_m}{u_m} L\left(\frac{j_m}{R}, k_\rho\right) L\left(\frac{j_n}{R}, k_\rho\right) k_\rho dk_\rho, \quad (\text{A8})$$

where,

$$L\left(\frac{j_q}{R}, k_\rho\right) = \int_0^R J_1\left(\frac{j_q}{R} \rho\right) J_1(k_\rho \rho) \rho d\rho.$$

Therefore, we can write the following matrix forms, which relates the magnetic current coefficients to the magnetic field coefficients:

$$\bar{B} = \bar{G}_R^{z_s} \bar{A}, \quad (\text{A9})$$

$$\bar{B}(n) = B_n, \bar{A}(n) = A_n, \quad (\text{A10})$$

$$\begin{aligned} \bar{G}_R^{z_s}(n, m) &= \frac{2k_0}{\eta_0 u_n u_m} \int_0^{k_0} \frac{e^{-ik_z z_s}}{k_z} L\left(\frac{j_m}{R}, k_\rho\right) \\ &\times L\left(\frac{j_n}{R}, k_\rho\right) k_\rho dk_\rho. \end{aligned} \quad (\text{A11})$$

Using Eq. (A9) in Eq. (A6), we write,

$$\langle R \rangle = 2\pi \left( \bar{A}^T \bar{G}_R^{z_s} \bar{A} \right). \quad (\text{A12})$$

The magnetic field  $\bar{H}(\rho, z = 0)$  in Eq. (A3), can be expanded similarly,

$$\bar{H}(\rho, z = 0) = \sum_{n=1}^N \frac{C_n}{u_n} J_1\left(\frac{j_n}{R} \rho\right) \hat{\phi}. \quad (\text{A13})$$

Substituting Eq. (A4) and Eq. (A13) into Eq. (A3), we have,

$$P = \frac{\pi}{2} \sum_{n=1}^N A_n C_n^*. \quad (\text{A14})$$

Using Eq. (A7) we can write,

$$\bar{C} = \bar{G}_R^0 \bar{A}, \quad (\text{A15})$$

$$\bar{C}(n) = C_n, \quad (\text{A16})$$

$$\bar{G}_R^0(n, m) = \frac{2k_0}{\eta_0 u_n u_m} \int_0^{k_0} \frac{1}{k_z} L\left(\frac{j_m}{R}, k_\rho\right) L\left(\frac{j_n}{R}, k_\rho\right) k_\rho dk_\rho. \quad (\text{A17})$$

Using Eq. (A15) in Eq. (A14), we write,

$$P = \frac{\pi}{2} \left( \bar{A}^T \bar{G}_R^0 \bar{A} \right). \quad (\text{A18})$$

Finally, by substituting Eqs. (A12) and (A18) into Eq. (A1) the coupling coefficients between two identical circular apertures can be written compactly in terms of the magnetic current coefficients as follows:

$$\Gamma = \frac{\left| \left( \bar{A}^T \bar{G}_R^{z_s} \bar{A} \right) \right|^2}{\left( \bar{A}^T \bar{G}_R^0 \bar{A} \right)^2}. \quad (\text{A19})$$

Equation (A19) is a special case of Eq. (A1) for the case of two opposing identical circular aperture antennas when the magnetic current distribution over the two apertures is written as a sum of orthogonal Bessel beams. The coefficients  $A_n^{z_s}$  are the ones that maximize the expression in Eq. (A19) for a given separation distance  $z_s$ . They can be found through optimization.

## APPENDIX B: CONDITION OF OPTIMAL ILLUMINATION

Here, we derive the condition of optimal illumination stated in Eq. (2) for coupling two identical circular aperture antennas, as shown in Fig. 2. Maximizing the coupling coefficient in Eq. (A19) is equivalent to maximizing the following inner product:

$$V = \bar{A}^T \bar{G}_R^0 \bar{G}_R^{z_s} \bar{A}. \quad (\text{B1})$$

By Schwarz's inequality, the sufficient condition to maximize  $V$  and accordingly  $\Gamma$  is,

$$\bar{G}_R^{z_s} \bar{A} = b \bar{G}_R^0 \bar{A}^*, \quad (\text{B2})$$

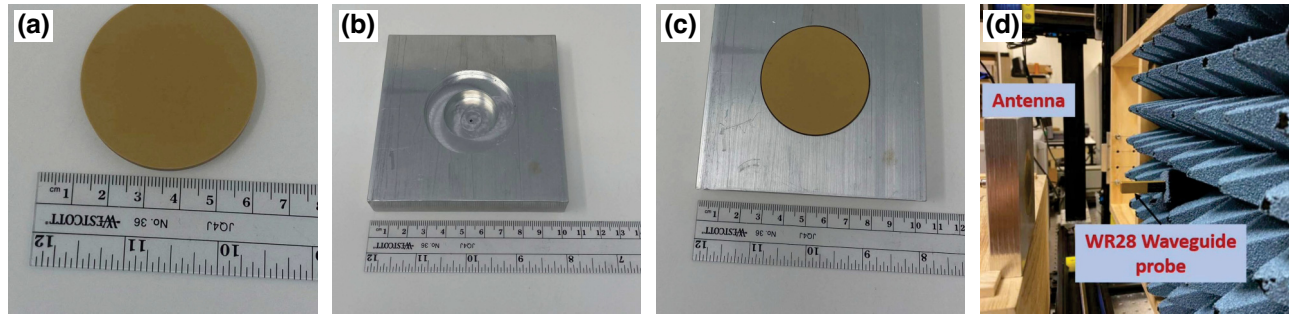


FIG. 11. Pictures of the fabricated RG antenna prototype and the measurement setup, (a) the cascaded-sheet, mode-converting metasurface by itself, (b) the machined cavity with a hole in the center for the coaxial connector, (c) the assembled antenna with the mode-converting metasurface atop the cavity, (d) measurement setup.

where,  $b$  is a complex constant. From Eqs. (A9), (A15) and Eq. (B2), we have,

$$\bar{B} = b \bar{C}^*. \quad (\text{B3})$$

Using Eqs. (A2), (A13) and Eq. (B3), it is straightforward to show that,

$$T(\rho)\bar{H}(\rho, z = z_s) = b T(\rho)\bar{H}^*(\rho, z = 0), \quad (\text{B4})$$

where,  $T(\rho \leq R) = 1$  and  $T(\rho > R) = 0$ . Substituting Eq. (B2) into Eq. (A19), we have,

$$\Gamma = |b|^2. \quad (\text{B5})$$

### APPENDIX C: FABRICATION AND MEASUREMENT SETUP

Pictures of the fabricated mode-converting metasurface and the machined cavity are shown in Figs. 11(a) and 11(b), respectively. Figure 11(c) shows a picture of the antenna once it is assembled. The cavity section and the feed transition were fabricated by machining a square 6061 aluminum plate to the dimensions given in Fig. 5(a). The dimensions of the 6061 aluminum plate is ( $4'' \times 4'' \times 3/4''$ ). These dimensions were chosen so that standard pre-cut aluminum plates can be used. The mode-converting metasurface was fabricated using standard PCB fabrication process. The metasurface layout is shown in Fig. 5(b). The minimum feature size of the mode-converting metasurface is larger than ( $0.003''$ ).

The antenna near field was measured using a standard rectangular WR28 ( $7.112 \text{ mm} \times 3.556 \text{ mm}$ ) waveguide probe, as shown in Fig. 11(d). The waveguide probe supports single-mode operation over the frequency range (26.5 to 40 GHz). The antenna far field was computed from the measured near field after probe compensation, as explained in Ref. [60].

- [1] D. Pohl, Operation of a ruby laser in the purely transverse electric mode  $\text{TE}_{01}$ , *Appl. Phys. Lett.* **20**, 266 (1972).
- [2] Y. Mushiake, K. Matsumura, and N. Nakajima, Generation of radially polarized optical beam mode by laser oscillation, *Proc. IEEE* **60**, 1107 (1972).
- [3] J. Durnin, Exact solutions for nondiffracting beams. I. The scalar theory, *J. Opt. Soc. Am. A* **4**, 651 (1987).
- [4] J. Durnin, J. Miceli Jr, and J. H. Eberly, Diffraction-free beams, *Phys. Rev. Lett.* **58**, 1499 (1987).
- [5] R. Herman and T. Wiggins, Production and uses of diffractionless beams, *J. Opt. Soc. Am. A* **8**, 932 (1991).
- [6] G. Indebetouw, Nondiffracting optical fields: Some remarks on their analysis and synthesis, *J. Opt. Soc. Am. A* **6**, 150 (1989).
- [7] M. Ettore and A. Grbic, Generation of propagating Bessel beams using leaky-wave modes, *IEEE Trans. Antennas Propag.* **60**, 3605 (2012).
- [8] D. McGloin and K. Dholakia, Bessel beams: Diffraction in a new light, *Contemp. Phys.* **46**, 15 (2005).
- [9] F. Alsolamy, W. A. Alomar, and A. Grbic, Cylindrical vector beams for wireless power transfer, *IEEE Trans. Antennas Propag.* **69**, 1716 (2020).
- [10] S. Quabis, R. Dorn, M. Eberler, O. Glöckl, and G. Leuchs, Focusing light to a tighter spot, *Opt. Commun.* **179**, 1 (2000).
- [11] R. Dorn, S. Quabis, and G. Leuchs, Sharper focus for a radially polarized light beam, *Phys. Rev. Lett.* **91**, 233901 (2003).
- [12] B. Jia, X. Gan, and M. Gu, Direct measurement of a radially polarized focused evanescent field facilitated by a single LCD, *Opt. Express* **13**, 6821 (2005).
- [13] R. H. Jordan and D. G. Hall, Free-space azimuthal paraxial wave equation: The azimuthal Bessel–Gauss beam solution, *Opt. Lett.* **19**, 427 (1994).
- [14] D. G. Hall, Vector-beam solutions of Maxwell’s wave equation, *Opt. Lett.* **21**, 9 (1996).
- [15] A. April, Bessel–Gauss beams as rigorous solutions of the Helmholtz equation, *J. Opt. Soc. Am. A* **28**, 2100 (2011).
- [16] Q. Zhan, Cylindrical vector beams: From mathematical concepts to applications, *Adv. Opt. Photonics* **1**, 1 (2009).

- [17] D. P. Biss, K. S. Youngworth, and T. G. Brown, Dark-field imaging with cylindrical-vector beams, *Appl. Opt.* **45**, 470 (2006).
- [18] F. O. Fahrbach, P. Simon, and A. Rohrbach, Microscopy with self-reconstructing beams, *Nat. Photonics* **4**, 780 (2010).
- [19] A. Novitsky, C.-W. Qiu, and H. Wang, Single gradientless light beam drags particles as tractor beams, *Phys. Rev. Lett.* **107**, 203601 (2011).
- [20] M. Meier, V. Romano, and T. Feurer, Material processing with pulsed radially and azimuthally polarized laser radiation, *Appl. Phys. A* **86**, 329 (2007).
- [21] V. R. Gowda, O. Yurduseven, G. Lipworth, T. Zupan, M. S. Reynolds, and D. R. Smith, Wireless power transfer in the radiative near field, *IEEE Antennas Wirel. Propag. Lett.* **15**, 1865 (2016).
- [22] J. D. Heeb, M. Ettore, and A. Grbic, Wireless links in the radiative near field via Bessel beams, *Phys. Rev. Appl.* **6**, 034018 (2016).
- [23] T. Grosjean, D. Courjon, and M. Spajer, An all-fiber device for generating radially and other polarized light beams, *Opt. Commun.* **203**, 1 (2002).
- [24] G. Volpe and D. Petrov, Generation of cylindrical vector beams with few-mode fibers excited by Laguerre–Gaussian beams, *Opt. Commun.* **237**, 89 (2004).
- [25] T. Hirayama, Y. Kozawa, T. Nakamura, and S. Sato, Generation of a cylindrically symmetric, polarized laser beam with narrow linewidth and fine tunability, *Opt. Exp.* **14**, 12839 (2006).
- [26] X. Yi, X. Ling, Z. Zhang, Y. Li, X. Zhou, Y. Liu, S. Chen, H. Luo, and S. Wen, Generation of cylindrical vector vortex beams by two cascaded metasurfaces, *Opt. Express* **22**, 17207 (2014).
- [27] Y. Xu, H. Zhang, Q. Li, X. Zhang, Q. Xu, W. Zhang, C. Hu, X. Zhang, J. Han, and W. Zhang, Generation of terahertz vector beams using dielectric metasurfaces via spin-decoupled phase control, *Nanophotonics* **9**, 3393 (2020).
- [28] M. Ettore, S. M. Rudolph, and A. Grbic, Generation of propagating Bessel beams using leaky-wave modes: Experimental validation, *IEEE Trans. Antennas Propag.* **60**, 2645 (2012).
- [29] F. Alsolamy and A. Grbic, Antenna aperture synthesis using mode-converting metasurfaces, *IEEE Open J. Antennas Propag.* **2**, 726 (2021).
- [30] O. Yurduseven and D. R. Smith, Dual-polarization printed holographic multibeam metasurface antenna, *IEEE Antennas Wirel. Propag. Lett.* **16**, 2738 (2017).
- [31] G. Minatti, F. Caminita, E. Martini, M. Sabbadini, and S. Maci, Synthesis of modulated-metasurface antennas with amplitude, phase, and polarization control, *IEEE Trans. Antennas Propag.* **64**, 3907 (2016).
- [32] A. Epstein and G. V. Eleftheriades, Synthesis of passive lossless metasurfaces using auxiliary fields for reflectionless beam splitting and perfect reflection, *Phys. Rev. Lett.* **117**, 256103 (2016).
- [33] B. O. Raeker and A. Grbic, Compound metaoptics for amplitude and phase control of wave fronts, *Phys. Rev. Lett.* **122**, 113901 (2019).
- [34] V. G. Ataloglou, A. H. Dorrah, and G. V. Eleftheriades, Design of compact Huygens' metasurface pairs with multiple reflections for arbitrary wave transformations, *IEEE Trans. Antennas Propag.* **68**, 7382 (2020).
- [35] O. Yurduseven, D. L. Marks, T. Fromenteze, and D. R. Smith, Dynamically reconfigurable holographic metasurface aperture for a mills-cross monochromatic microwave camera, *Opt. Express* **26**, 5281 (2018).
- [36] F. Alsolamy and A. Grbic, in *2020 Fourteenth International Congress on Artificial Materials for Novel Wave Phenomena (Metamaterials)* (IEEE, New York, 2020), p. 75.
- [37] F. Alsolamy and A. Grbic, Modal network formulation for the analysis and design of mode-converting metasurfaces in cylindrical waveguides, *IEEE Trans. Antennas Propag.* **69**, 4598 (2021).
- [38] M. Almunif, J. Budhu, and A. Grbic, Design of Beamforming, Transparent Metasurfaces Using Integral Equations, *arXiv:2310.05965v1* [physics.app-ph] (2023).
- [39] K. Shastri and F. Monticone, Nonlocal flat optics, *Nat. Photonics* **17**, 36 (2023).
- [40] C. L. Holloway, E. F. Kuester, J. A. Gordon, J. O'Hara, J. Booth, and D. R. Smith, An overview of the theory and applications of metasurfaces: The two-dimensional equivalents of metamaterials, *IEEE Antennas Propag. Mag.* **54**, 10 (2012).
- [41] A. Epstein and G. V. Eleftheriades, Arbitrary power-conserving field transformations with passive lossless omega-type bianisotropic metasurfaces, *IEEE Trans. Antennas Propag.* **64**, 3880 (2016).
- [42] J. G. N. Rahmeier, T. J. Smy, J. Dugan, and S. Gupta, Zero Thickness surface susceptibilities and extended GSTCs—part I: Spatially dispersive metasurfaces, *IEEE Trans. Antennas Propag.* **71**, 5909 (2023).
- [43] T. J. Smy, J. G. N. Rahmeier, J. Dugan, and S. Gupta, Spatially dispersive metasurfaces—part II: IE-GSTC-SD field solver with extended GSTCs, *IEEE Trans. Antennas Propag.* **71**, 5920 (2023).
- [44] S. Paković, S. Zhou, D. González-Ovejero, S. C. Pavone, A. Grbic, and M. Ettore, Bessel–Gauss beam launchers for wireless power transfer, *IEEE Open J. Antennas Propag.* **2**, 654 (2021).
- [45] J. Richmond, A reaction theorem and its application to antenna impedance calculations, *IRE Trans. Antennas Propag.* **9**, 515 (1961).
- [46] G. v. Borgiotti, Maximum power transfer between two planar apertures in the Fresnel zone, *IEEE Trans. Antennas Propag.* **14**, 158 (1966).
- [47] C. Pfeiffer and A. Grbic, Controlling vector Bessel beams with metasurfaces, *Phys. Rev. Appl.* **2**, 044012 (2014).
- [48] M. Albani, S. Pavone, M. Casaletti, and M. Ettore, Generation of non-diffractive Bessel beams by inward cylindrical traveling wave aperture distributions, *Opt. Express* **22**, 18354 (2014).
- [49] M. Martinis, L. Bernard, K. Mahdjoubi, R. Sauleau, and S. Collardey, Wideband antenna in cavity based on metasurfaces, *IEEE Antennas Wirel. Propag. Lett.* **15**, 1053 (2015).
- [50] A. Epstein, J. P. Wong, and G. V. Eleftheriades, Cavity-excited Huygens' metasurface antennas for near-unity aperture illumination efficiency from arbitrarily large apertures, *Nat. Commun.* **7**, 1 (2016).
- [51] D. L. Marks, O. Yurduseven, and D. R. Smith, Cavity-backed metasurface antennas and their application

- to frequency diversity imaging, *J. Opt. Soc. Am. A* **34**, 472 (2017).
- [52] F. Bowman, in *Introduction to Bessel Functions* (Dover, New York, 1958), p. 101.
- [53] The coefficients are normalized such that  $[A_1^{zs}, \dots, A_5^{zs}] [A_1^{zs}, \dots, A_5^{zs}]^\dagger = 1$ .
- [54] The coefficients are normalized such that  $[A_1^{\text{RG}}, \dots, A_5^{\text{RG}}] [A_1^{\text{RG}}, \dots, A_5^{\text{RG}}]^\dagger = 1$ .
- [55] C. Pfeiffer and A. Grbic, Metamaterial Huygens' surfaces: Tailoring wave fronts with reflectionless sheets, *Phys. Rev. Lett.* **110**, 197401 (2013).
- [56] D. Zaluški, A. Grbic, and S. Hrabar, Analytical and experimental characterization of metasurfaces with normal polarizability, *Phys. Rev. B* **93**, 155156 (2016).
- [57] The coefficients are calculated using the full-wave solver ANSYS-HFSS.
- [58] M.-K. Hu, Near-zone power transmission formulas, IRE Nat'l Conv. Rec. **6**, 128 (1958).
- [59] V. Rumsey, Reaction concept in electromagnetic theory, *Phys. Rev.* **94**, 1483 (1954).
- [60] D. Paris, W. Leach, and E. Joy, Basic theory of probe-compensated near-field measurements, *IEEE Trans. Antennas Propag.* **26**, 373 (1978).